Exsolution of Embedded Nanoparticles in Defect Engineered Perovskite Layers

Moritz L. Weber [a, b, c, d,*], Marek Wilhelm [e], Lei Jin [c, f], Uwe Breuer [g], Regina Dittmann [b, c], Rainer Waser [b, c, h], Olivier Guillon [a, d, i], Christian Lenser [a,*] and Felix Gunkel [b, c,*]

[a] Institute of Energy and Climate Research (IEK-1), Forschungszentrum Juelich GmbH, 52425 Juelich, Germany [b] Peter Gruenberg Institute (PGI-7), Forschungszentrum Juelich GmbH, 52425 Juelich, Germany [c] Juelich-Aachen Research Alliance (JARA-FIT), 52425 Juelich, Germany [d] Institute of Mineral Engineering (GHI), RWTH Aachen University, 52062 Aachen, Germany [e] Peter Gruenberg Institute (PGI-6), Forschungszentrum Juelich GmbH, 52425 Juelich, Germany [f] Ernst Ruska-Centre for Microscopy and Spectroscopy with Electrons (ER-C), Forschungszentrum Juelich GmbH, 52425 Juelich, Germany [g] Central Institute for Engineering, Electronics and Analytics (ZEA-3), Forschungszentrum Juelich GmbH, 52425 Juelich, German [h] Institute for Electronic Materials II (IWE II), RWTH Aachen University, 52056 Aachen, Germany [i] Juelich-Aachen Research Alliance (JARA-Energy), 52425 Juelich, Germany

ABSTRACT: Exsolution phenomena are highly debated as efficient synthesis route for nanostructured composite electrode materials for the application in solid oxide cells (SOCs) and the development of next-generation electrochemical devices for energy conversion. Utilizing the instability of perovskite oxides, doped with electrocatalytically active elements, highly dispersed nanoparticles can be prepared at the perovskite surface under influence of a reducing heat treatment. For the systematic study of the mechanistic processes governing metal exsolution, epitaxial $SrTi_{0.9}Nb_{0.05}Ni_{0.05}O_{3-\delta}$ thin films of well-defined stoichiometry are synthesized and employed as model systems to investigate the interplay of defect structures and exsolution behavior. Spontaneous phase separation and the formation of dopant-rich features in the as-synthesized thin film material is revealed by high-resolution transmission electron microscopy (HR-TEM) investigations. The resulting nanostructures are enriched by nickel and serve as pre-formed nuclei for the subsequent exsolution process under reducing conditions, which reflects a so far unconsidered process drastically affecting the understanding of nanoparticle exsolution phenomena. Using an approach of combined morphological, chemical and structural analysis of the exsolution response, a limitation of the exsolution dynamics for non-stoichiometric thin films is found to be correlated to a distortion of the perovskite host lattice. Consequently, incorporation of defect structures results in a reduced particle density at the perovskite surface, presumably by trapping of nanoparticles in the oxide bulk.

KEYWORDS: metal exsolution, metal nanoparticles, oxide epitaxy, atomic engineering, nanoparticle transport, transport dynamics

Efficient energy conversion and energy storage is the key element of a sustainable energy management and steadily gains in importance due to the increasing focus on climate-neutral energy production. Here, solid oxide electrolyzer cells (SOECs) and solid oxide fuel cells (SOFCs), which enable dynamic energy generation and storage, are promising candidates to address the spatial and temporal mismatch between energy production and energy consumption.[1–5] However, a major challenge in the field is the development of high-performance electrode materials to increase applicability of these electrochemical devices. Nanostructuring of functional materials has been established as a valuable approach to improve the electrochemical performance, for example through modification of the chemical and electronic properties to tailor the reaction pathways, or by increasing the active surface area.[6–11] In particular, supported catalyst nanoparticles, providing for highly dispersed and accessible catalytic centers, take a vital role for the design of functional materials as substantial components in electrochemical devices. Recently, redox exsolution has been proven an efficient strategy for the synthesis of self-assembled nanostructures which can serve as functional composite materials with increased activity and stability of the nanoparticle electrocatalysts.[12–16] Exsolution processes can be considered as partial decomposition of perovskite oxides by exceeding the thermodynamic stability limits under chemical gradients and at elevated temperatures or applied potential.[17,18] The resulting metallic secondary phase, consisting of the respective dopants, is present as highly dispersed and stable nanoparticles within the remaining oxide support and at the oxide surface providing for well-accessible electrocatalytic centers. Hence, fabrication of nanocomposites *via* redox exsolution may play a decisive role to further decrease operation temperatures in low-temperature SOC applications, considered an essential need to achieve wide-ranging implementation of SOC technologies, which allow for flexible and sustainable energy storage and energy conversion.

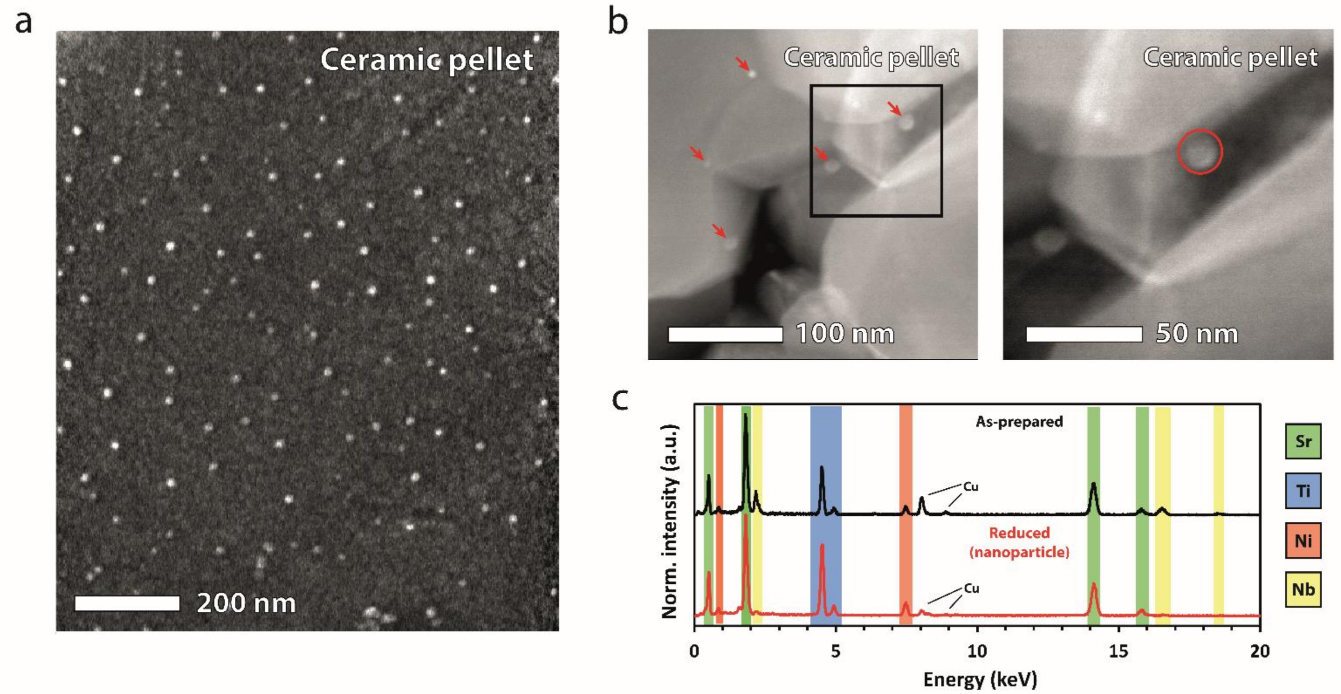

Figure 1. Microscopic analysis of a sintered ceramic pellet of $SrTi_{0.9}Nb_{0.05}Ni_{0.05}O_{3-\delta}$ after thermal treatment under reducing conditions (annealing conditions: 5h / Ar / 4 % H_2 / 800°C). (a) Scanning electron microscopy (SEM) imaging shows the formation of nanoparticles at the polished surface of the oxide ceramic. (b) Scanning transmission electron microscopy (STEM) reveals exsolved nanoparticles at the surface of the oxide grains analyzed in dark-field imaging mode. Several exsolved nanoparticles are highlighted by red arrows in the TEM image (left panel) and the area of magnification equal to the right panel is indicated by the black square. (c) The enrichment of nickel is detected by means of energy dispersive X-ray spectroscopy (EDXS) comparing point scans obtained from the oxide precursor in the as-prepared state and from an exsolved nanoparticle in the reduced state of the sample. Please note that the Cu-signal originates from the TEM sample holder.

The effective use of metal exsolution for the preparation of catalysts and the precise control of specific particle properties - such as particle density - requires profound knowledge about the atomistic processes during redox exsolution. Recent reports have highlighted the importance of the perovskite defect structure for metal exsolution. For instance, A-site deficiency of the respective perovskite structure ABO_3 was shown to significantly promote nanoparticle formation at the surface of perovskite materials (rather than remaining in the oxide bulk) and has established a powerful strategy to control nanoparticle formation.[19–21] Other studies have indicated the influence of extended defect structures such as stacking faults within the as-synthesized perovskite host lattice, which were reported to act as preferential sites for nanoparticle formation.[22] Also an effect of non-stoichiometry on electrochemical performance with respect to the formation of secondary phases and distortion of the host lattice accompanied by redox exsolution was discussed.[23]

Furthermore, it was shown that mass transport to the oxide surface may be related to lattice strain between metal nanoparticles forming in the bulk and the surrounding oxide lattice providing for high mobility of metallic species.[24,25] However, little is known about the exact pathways of mass transport during nanoparticle nucleation in the oxide bulk and the interplay between exsolving metal species with structural defects present within the oxide lattice. In particular, the investigation of strongly entangled surface and bulk processes involved in nanoparticle formation and transport is of high interest to improve the understanding of the fundamental processes underlying metal exsolution. In this paper, we will therefore disentangle nucleation and transport of the nanoparticles to investigate the influence of defect structures on the directed nanoparticle transport towards the perovskite surface.

$SrTi_{0.9}Nb_{0.05}Ni_{0.05}O_{3-\delta}$ (STNNi) shows a high affinity for metal exsolution. As can be seen, reducing thermal treatment results in formation of nanoparticles at the surface of the ceramic oxide pellet (Fig. 1a) as well as at single powder grains as revealed by investigations of the ceramic microstructure (Fig. 1b), which can be identified to be enriched by Ni (Fig. 1c). However, the inherent structural complexity of technical ceramic components (*e.g.* porosity, grain size distributions, crystal orientation, grain boundaries) complicates the fundamental investigation of complex exsolution processes that involve the exchange of oxygen, cation migration and cation interaction in a wide temperature- and pressure range since the microstructure needs to be accurately accounted for in order to assess material properties.

Here, we employ epitaxial STNNi thin films as model systems for the investigation of subsurface nucleation and nanoparticle transport processes during metal exsolution from close-to atomically defined oxides with defined crystal structure and orientation, as well as precisely defined stoichiometry and defect structure. Notably, microscopic investigations reveal the (partial) phase separation of NiO_x and the host oxide. Nano-sized secondary structures are present in the as-prepared perovskite host lattice serving as pre-formed nuclei for metal exsolution under reducing treatment, so that nanoparticle formation does not take place from individual ions. In a second step, epitaxial growth is used as a tool to systematically engineer the defect structure of the perovskite host lattice to study the interplay of defects with the nanoparticle transport to the oxide surface. Defect-induced lattice distortions are found to have significant impact on the exsolution of pre-formed nuclei where both A-site excess and A-site deficiency of the perovskite host lattice appears to slow or trap nanoparticles within the thin film bulk and hence hamper nanoparticle transport towards the crystal surface.

RESULTS AND DISCUSSION

Material synthesis and characterization of the exsolution response.

The prototype transition metal oxide $SrTiO_3$ was chosen as host material for the investigation of the redox exsolution behavior of nickel as it exhibits a strong response to reducing thermal treatment resulting in the formation of metallic nanoparticles at the oxide surface as summarized in the introduction (cf. Fig. 1). Furthermore, it is considered a promising candidate for the application in full ceramic SOFC designs.[26–28] The optimal doping level in terms of maximum Ni concentration and phase purity is determined by variation of the Ni-substitution and respective X-ray diffraction (XRD) analysis of sintered ceramic pellets (cf. Supporting Information (SI) Fig. S1). Here, Ni-doping up to 5% at the perovskites B-site was found to be accommodated without formation of visible secondary phases, while increasing Ni-substitution results in the formation of a NiO secondary phase. Complementary TEM investigations of a representative sample of 5% Ni-doping did not reveal any significant secondary phases in the ceramic compound (cf. Fig. S2). Epitaxial growth of Ni- and Nb-substituted strontium titanate on single-crystalline STO substrates is controlled *via* reflection high-energy electron diffraction (RHEED) by monitoring of the (0 0) specular spot of the surface diffraction pattern (cf. inset, Fig. 2a), revealing intensity oscillations over the entire deposition time (Fig. 2a). Consequently, STNNi thin films are deposited in layer-by-layer (*i.e.* two-dimensional) growth mode and with monolayer precision (50 nm equals ~128 monolayers of STNNi; typically 128 oscillations can be observed during deposition). Consistent with the 2D RHEED pattern (inset, Fig. 2a) obtained from the as-grown layer, thin film morphology exhibits a well-defined step terrace structure with generally low surface roughness, typically in the sub-nanometer range (Fig. 2b) as revealed by atomic force microscopy (AFM). Fig. 2c displays the SIMS (Secondary ion mass spectrometry) depth profile of an as-prepared STNNi thin film. Note that for the purpose of SIMS analysis the sample was covered with $t = 30$ nm of evaporated platinum to reduce irregular sputtering effects at the surface. A steep increase in secondary ion intensity of niobium and nickel is evident crossing the platinum to thin film interface while loss in intensity indicates the sharp interface between thin film material and STO substrate. As can be seen, sputter profiles exhibit constant intensities for all involved cations, providing information about their macroscopically uniform distribution over the entire thin film thickness. Furthermore, high crystallinity of the thin film material is visible from XRD analysis. Evidently, STNNi thin films are synthesized in a single orientation of the perovskite structure showing no detectable secondary phases in wide-angle XRD analysis (cf. Fig. S3a). As can be seen from Fig. 2d, the (002) thin film reflection is visible at lower diffraction angles compared to the (002) reflection of the strontium titanate substrate indicating a slight expansion of the STNNi crystal lattice in *c*-direction, which is typically associated with extrinsic doping[29] or defect formation.[30–33] Both, 2θ-ω scan and reciprocal space map (RSM) exhibit periodic oscillations (Kiessig fringes) in the vicinity of the thin film reflections, indicating a sharp interface between the thin film and the STO substrate (see Fig. 2d,e). In fact, the specific structural characteristics (*i.e.* expansion of the *c*-axis) of the present material system is not only based on the steric and electrostatic interaction due to extrinsic doping as well as minor compressive strain in consequence of the epitaxial relationship with the underlying substrate and potential presence of cationic defects, but results from a more complex material property as will be discussed later on.

After thermal treatment under reducing conditions (15h / Ar/4% H_2 / 800°C), formation of particles with high coverage and a particle height between 15 nm - 30 nm (see line profile as inset image) is visible at the surface (Fig. 3a). The particles evolve from highly defined and smooth crystal surfaces, while the step terrace structure of the host oxide is preserved during annealing and only minor morphological changes apart from particle formation are visible at the present annealing conditions. These findings therefore demonstrate the high affinity of the material system to form exsolution particles as well as the stability of the host material under annealing conditions. Consistent with morphological investigations, XRD analysis obtained in the as-prepared and reduced state of the model system reveals only slight changes in the diffractograms, which in general indicates a high robustness of the host oxide with respect to the annealing treatment (Fig. 3b). A considerable shift in the position of the (002) thin film reflection towards higher 2θ-angles (relative to the (002) substrate reflection) can be observed, resulting from a relaxation in the *c*-lattice parameter.

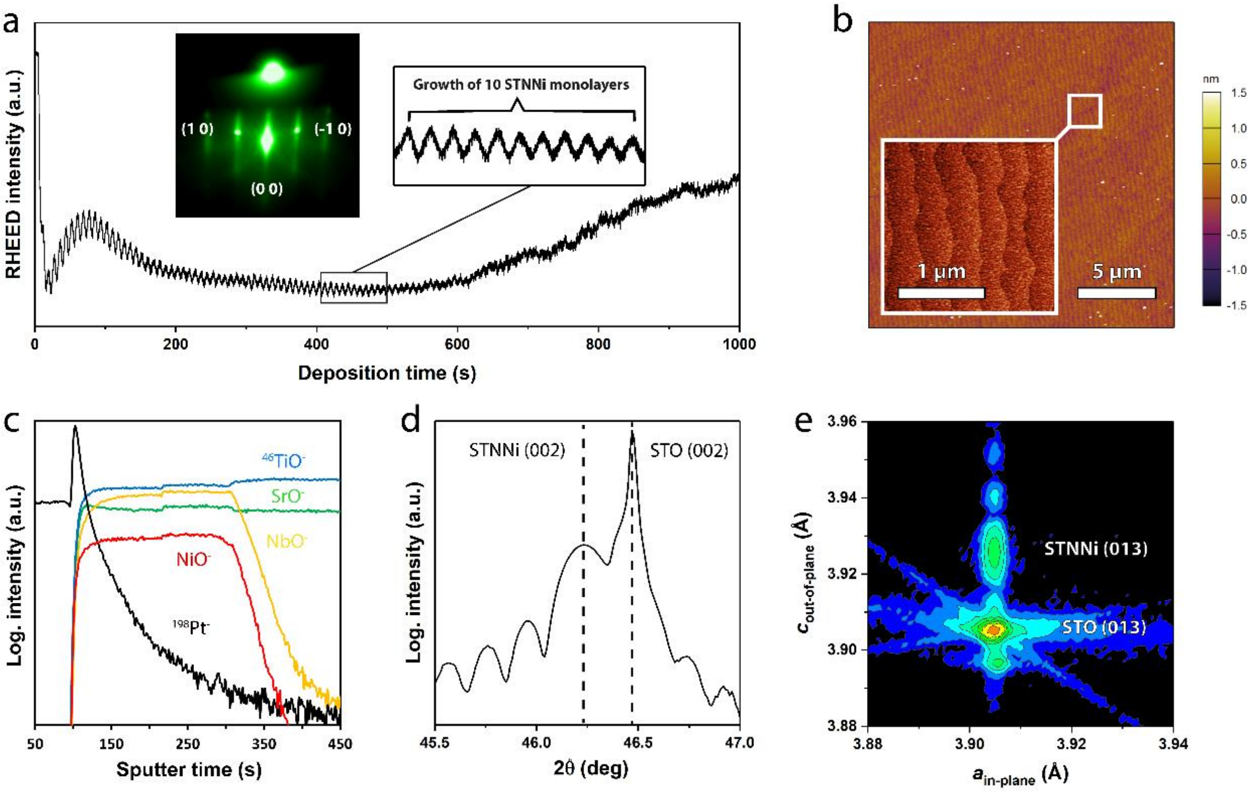

Figure 2. Epitaxial growth characteristics and material properties of a representative, stoichiometric STNNi thin film of 50 nm thickness. (a) Intensity evolution of the RHEED specular spot (00) during PLD growth indicating layer-by-layer deposition and (inset image, left) corresponding surface diffraction pattern as well as (inset image, right) close-up of intensity oscillations highlighting the deposition of ten monolayers of the material. (b) Surface morphology of as-prepared epitaxial STNNi thin films (scan size 20 x 20 µm^2 and inset 2 x 2 µm^2). (c) Cation distribution profiles obtained by SIMS analysis. X-ray diffraction analysis (d) in the (002) STNNi/STO region and (e) reciprocal space map recorded around the (013) reflection.

The apparent shift is frequently linked to the release of dopants from the perovskite host lattice although it might be superimposed with further processes induced by the reducing treatment. For instance, formation of cation and oxygen vacancies (chemical expansion[34,35]) and the respective change of the transition metal valence state may influence the crystallographic properties and contribute the overall apparent peak shift with partly contrary effect. Further influence on the out-of-plane lattice parameter originates from the particular structural characteristics of the present material system as will be elaborated in the following discussion. Please note, that no change in the in-plane lattice parameter is observed by RSM and hence no relaxation of the epitaxial strain results from the annealing procedure at elevated temperatures (cf. Fig. S3b). Here, low lattice misfit between STNNi thin films and the STO substrate ensures very low strain energies and consequently negligible influence of epitaxial strain (introduced by epitaxial growth) on the exsolution process.[24] Consistent with surface characterization, XRD analysis confirms the high stability of the host lattice during exsolution.

The sample geometry furthermore allows for the analysis of surface chemistry by surface-sensitive X-ray photoelectron spectroscopy (XPS). Here, relative cation stoichiometry is quantified based on relative areas of the respective core-level spectra after calibration to the stoichiometry of the target used for PLD (representative core-level spectra are shown in the SI, Fig. S4). By comparison of the as-prepared and reduced state of STNNi thin films, considerable changes in the sample stoichiometry are detected (Fig. 3c). Most prominently, a significant enrichment of nickel in the surface region is evident. Therefore, morphologic changes revealed by surface characterization can be clearly assigned to the formation of Ni nanoparticles.

To confirm the formation of metallic nanoparticles, vibrating sample magnetometry (VSM) can be applied to characterize the magnetic transition, comparing the as-prepared and reduced state of the material (Fig. 3d) as recently demonstrated for the quantitative analysis of exsolution nanoparticles.[36]

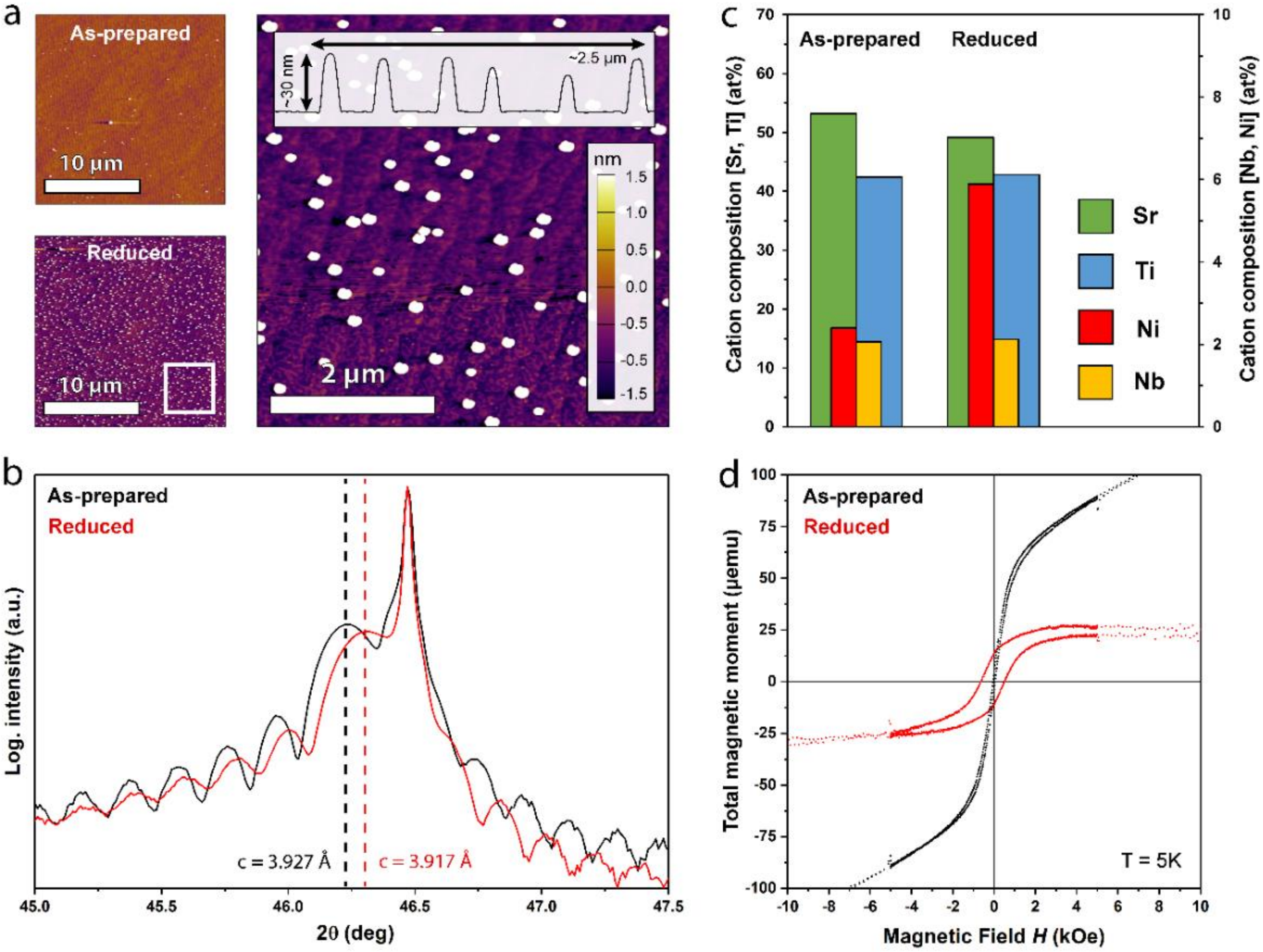

Figure 3. Characterization of a representative stoichiometric STNNi thin film comparing the as-prepared and reduced state (annealing conditions: 15h / Ar/4% H_2 / 800°C). Surface morphology of epitaxial STNNi thin films in the (a) as-prepared state (scan size 20 x 20 µm^2); and below in the reduced state (scan size 20 x 20 µm^2). Close up of the surface morphology of the reduced state is equal to the area indicated by the white frame (scan size of 5 x 5 µm^2) and (inset image above) line profile across exsolution particles. (b) X-ray diffraction analysis in the (002) STNNi/STO region revealing a shift in the lattice parameter due to the reducing annealing procedure. (c) Relative cation stoichiometry in the surface region determined by XPS analysis; color code is given alongside the figure. (d) Total magnetic moment as a function of the applied external magnetic field *H* measured at a temperature of $T = 5$ K obtained from as-prepared and reduced thin films. The transition in the magnetic signature gives evidence about a change in Ni oxidation state and the formation of metallic Nickel nanoparticles (covered by a NiO passivation layer).

The diagram shows the total magnetic moment as a function of the applied external magnetic field *H* measured at a temperature of $T = 5$ K. The hysteresis loop of the as-prepared state reveals a small coercive field of $H_C = 50$ Oe and the magnetic moment does not saturate, which may indicate superparamagnetic behavior. This result is in line with various studies of antiferromagnetic NiO nanoparticles, which exhibit a superparamagnetic relaxation of their spin lattices as well as permanent magnetic moments arising from uncompensated surface spins.[37–39] The red coloured hysteresis loop represents the reduced state, which reveals a clear ferromagnetic signal indicated by a significantly larger coercive field of $H_C = 570$ Oe. The ferromagnetic response is attributed to the formation of metallic Ni nanoparticles.

Atomic-scale analysis of the structural properties.

Nucleation of metallic nanoparticles was reported to proceed in the oxide bulk (subsurface region) upon reduction and to be subsequently released to the perovskite surface.[24,25,40] To unveil the atomistic processes involved in nanoparticle nucleation and growth, transmission electron microscopy (TEM) investigations of a representative stoichiometric thin film along the [001] direction were performed, comparing the as-prepared and the reduced state. Surprisingly, TEM dark-field imaging reveals inhomogeneities in the thin film bulk and the presence of secondary structures on the nanometer-scale embedded at designated regions of the as-synthesized STNNi perovksite lattice (Fig. 4a). These column-like nanostructures were identified to be enriched by nickel by means of chemically sensitive energy dispersive

X-ray spectroscopy (EDXS) and hence may be related to spontaneous phase separation (Fig. 4b). Considering the layer-by-layer thin film growth and the well-defined surface and bulk properties of the STNNi thin film model systems (cf. Fig. 2) this observation is rather striking. The small size of the nanostructures and the fine lateral dispersion within the host lattice is likely to have prevented their detection by the applied characterization techniques discussed above. This observation is contradictory to the expectation of nanoparticle formation from Ni-dopants occupying specific crystallographic sites of the perovskite structure.

Fig. 4c shows the high-angle annular dark-field (HAADF) scanning TEM (STEM) images of the as-prepared and annealed STNNi thin films, respectively. In HAADF imaging condition high Z-atomic numbers yield high intensity and Ni accumulation results in bright contrast. On the atomic scale, the embedded Ni-rich phase with a column-like structure and rather undefined dimensions shows a transformation after the reducing heat treatment to a capsule-shaped nanocluster of clear perimeter (Fig. 4c). The surrounding host lattice however exhibits high coherency in the atomic ordering with no apparent differences in the as-prepared and the reduced state of the sample. EDXS measurements of the elemental distribution in the reduced state of the sample furthermore shows solely changes in the Ni-signal while the signals of the other cations appear to remain constant (cf. Fig. S5). The superposition of different crystallographic phases is furthermore evident from the fast-Fourier transforms (FFT) of the Z-contrast images. Here, satellite spots in the vicinity of the main diffraction spots of the host lattice originate from double diffraction and result in the emergence of a Moiré pattern (cf. Fig. S6) corresponding to the translational Moiré pattern visible in the real space images (Fig. 4c). These intensity modulations are more pronounced for the reduced state of the sample, while only faint (and fewer) satellite spots can be observed for the as-prepared state. This indicates a change in the orientation relationship between the embedded nanostructures and the host lattice with respect to zone axis as well as increased crystallinity of the nanocluster. The difference in the orientation relationship can be either explained by a change in the orientation of the embedded phase or by phase transition. To further clarify the structural (and chemical) nature of the embedded Ni-rich nanostructures, selected area electron diffraction (SAED) is applied. Since the observed Moirè pattern is a direct result of dynamic scattering events at the superimposed crystallographic planes, the periodicity of the modulated intensity spots provides information about the lattice spacing in the projected orientation of the crystal phases and may help to identify the embedded phase and its structural relationship with the host lattice (Fig. 4d).

Using the lattice parameter of the host oxide lattice (determined by XRD analysis) as internal reference allows to determine possible values for the lattice spacing of the embedded phases from the diffraction pattern as summarized in the SI (cf. Tab. S1). Based on the lattice parameters as reference point and by considering the (oxidizing) deposition conditions as well as (reducing) annealing conditions, NiO_x and metallic Ni were identified as most plausible candidates to be present as embedded phases in the as-prepared and reduced state of the sample. To further evaluate consistency of the suggested material compositions, models of the respective Moiré patterns were simulated for overlapping NiO/STO and Ni/STO, which are in good agreement with the experimentally observed periodicity of intensity modulations in real space (cf. Fig. S7). The respective nanostructures compose a system of large lattice misfit with the surrounding oxide host lattice and thus are expected to form a semicoherent interface based on domain matching epitaxy to relieve the strain energy resulting from the large natural misfit of their lattice parameters. The interface superstructure can be described by a coincidence site lattice (CSL) model with $n \times d_{\mathrm{host}} = (n \pm 1) \times d_{\mathrm{embedded}}$ and hence n spacings of the host lattice match with $n \pm 1$ spacings of the crystal lattice of the respective embedded phase.[41–44] Here, a registry of $n = 15$ unit cells of NiO matches a registry of $n = 16$ unit cells of the oxide host lattice, while in the reduced state a registry of $n = 12$ unit cells of the metallic nickel nanoclusters can be found to match a registry of $n = 11$ unit cells of the host lattice. Please note, that the determined domain matching registry results in a modified visible (half-order) periodicity of 7.5 : 8 unit cells in the as-prepared and 5.5 : 6 unit cells in the reduced state as visualized in Fig. S7. Based on the residual mismatch of the respective domains the minimum CSL misfit can be determined by $F_{CSL} = 1 - ((n + 1) \times d_{\mathrm{host}}) / (n \times d_{\mathrm{embedded}})$ which is equal to $F_{CSL} \sim 0.18$ % for the as-prepared and $F_{CSL} \sim -0.1$ % for the reduced state of the material system. Hence, low residual strain results from imperfect domain matching which may be compensated by elastic deformation of the crystal lattice.

Here, the extent of elastic deformation in each of the involved phases depends on the minimum CSL misfit, the elastic stiffness tensors and the interfacial area as well as dislocation density.[43] This may result in additional expansion in the *c*-lattice of the host oxide, as reported for a similar material system (perovskite phase $La_{0.7}Sr_{0.3}MnO_3$ and binary oxide MgO) and depends on the volume fraction of the embedded phase.[43] The out-of-plane lattice parameter of epitaxial STNNi thin films is hence not fully conclusive as an indicator for the incorporation and release of Ni-dopants as it is determined by various aspects *e.g.* the doping level, the (horizontal) strain with the substrate as well as the structural properties of the vertical interface. The apparent shift of the thin film reflection comparing the as-prepared and reduced state of the sample (cf. Fig. 3b) thus may be partially caused by reconstruction of the semicoherent interface by undergoing a phase transition from the oxidized to the reduced state *i.e.* changing from an oxide-oxide to an oxide-metal interface.

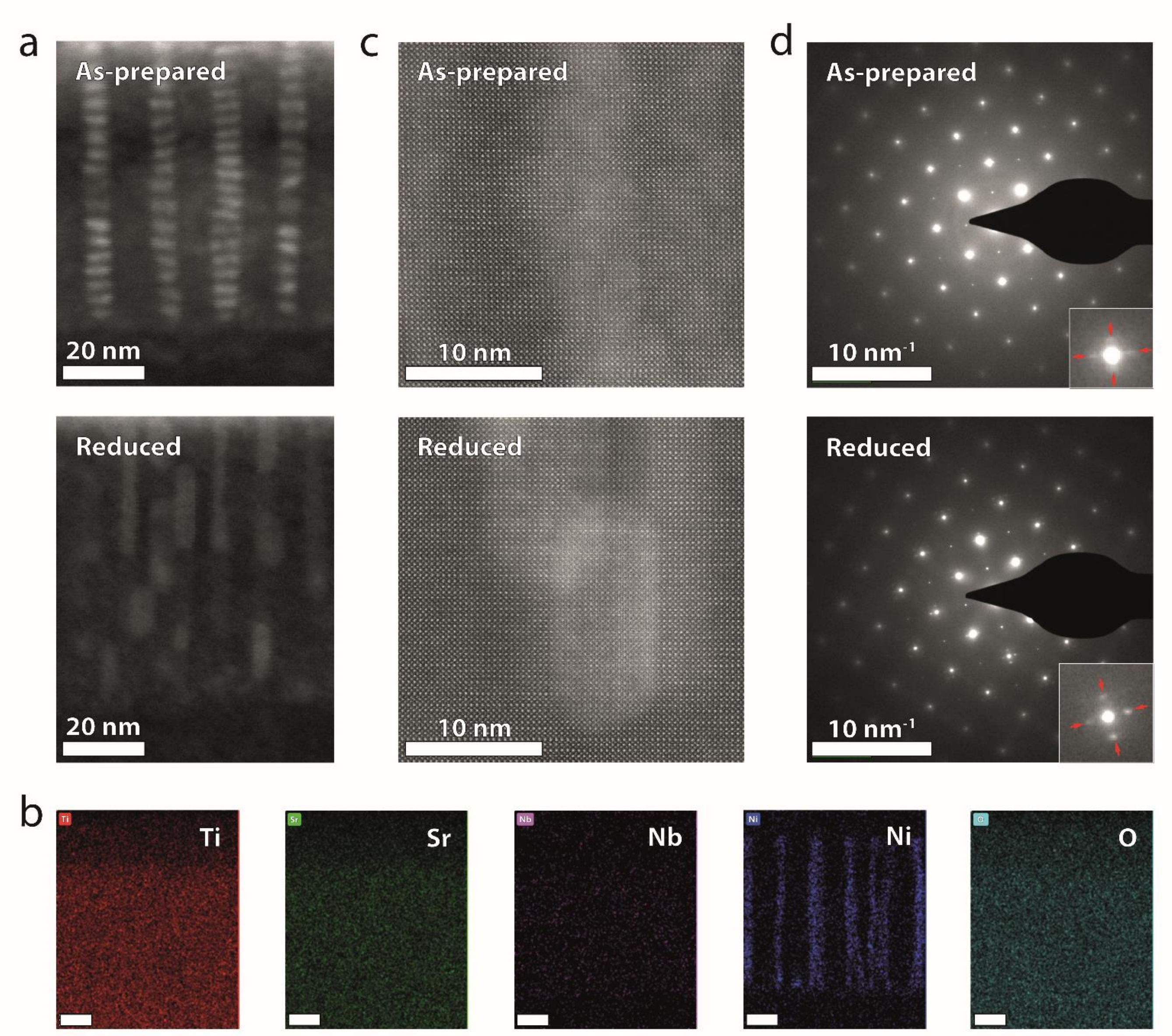

Figure 4. Transmission electron microscopy (TEM) analysis for a representative, stoichiometric STNNi thin film of 100 nm thickness deposited on an (001) STO substrate using a laser fluence of $F = 1.14\ \mathrm{J \cdot cm^{-2}}$. (a) Investigations in dark-field imaging reveals the presence of inhomogeneities in the as-prepared thin films in the form of column-like nanostructures embedded in the perovskite lattice. After annealing under reducing conditions an altered distribution of the embedded phase and partial depletion of nickel is visible. (b) Enrichment of Ni-dopants within the nanostructures is detected by means of EDXS analysis, here shown for the as-prepared state of the sample; scale-bars denote 20 nm. (c) Imaging of the atomic structure in high-annular angle dark-field imaging mode shows a detailed scan of the Ni-rich phase embedded in the STO host lattice in the as-prepared and reduced state of the sample. Reorganization of the crystalline order upon sample annealing and the formation of a nanocluster of clear perimeter is visible. (d) Electron diffraction patterns recorded from the as-prepared and the reduced state of the sample. Intensity modulations as results of double diffraction are visible as satellite spots around the main diffraction spots. Close-up images of a representative diffraction spot with satellite spots are given as inset (satellite spots are highlighted by red arrows).

Control of the exsolution strength by defect engineering.

To investigate the influence of non-stoichiometry *i.e.* defect incorporation on the exsolution behavior epitaxial growth is used to engineer the defect structure of the perovskite thin films. A convenient strategy to control the defect structure of complex oxides, ablating from a stoichiometric oxide target, is to tune the laser fluence applied during PLD growth.[45–50] This approach allows to systematically vary and introduce cation non-stoichiometry and the corresponding defect structures compensating for deviations from the nominal stoichiometry in the perovskite lattice based on the kinetically determined (*i.e.* non-equilibrium) growth process. For epitaxially deposited strontium titanate (STO) thin films, it was shown that moderate non-stoichiometry of the oxide is primarily balanced by the Sr-sublattice. Here, Sr-excess relative to the nominal stoichiometry is accommodated by the intergrowth of additional SrO planes *i.e.* the formation of Ruddlesden-Popper type defects[33,51], while Sr-depletion was shown to be compensated by the accumulation of Sr-vacancies forming vacancy clusters at large vacancy concentrations.[32,47] Hence, accommodation of non-stoichiometry is accompanied by the formation of distinct defect structures within the perovskite lattice.

STNNi thin films of varying defect structure were deposited with laser fluences in the range of $F = 0.88\ \mathrm{J{\cdot}cm^{-2}} - 1.44\ \mathrm{J{\cdot}cm^{-2}}$, while the stoichiometry of the host lattice was investigated by means of XPS analysis. As can be seen, a variation of laser fluence allows for the control of the Sr/(Sr+Ti) ratio in the surface region of the thin film model systems (Fig. 5a) as well as the thin film bulk (cf. Fig. S4b). Please note, that the formation of self-assembled Ni-rich nanostructures as described above was observed independent from thin film stoichiometry. The systematic variation of thin film stoichiometry is accompanied by a slight shift in the diffraction angle of the (002) thin film reflection observed in 2θ-ω scans (respectively for increasing Sr-deficiency and Sr-excess). Hence, incorporation of non-stoichiometry in form of defects within the perovskite lattice is evident by an expansion of the *c*-lattice in reference to stoichiometric STNNi due to the introduction of strain to the crystal lattice (Fig. 5b; diffractograms displayed in Fig. S8).[30–33]

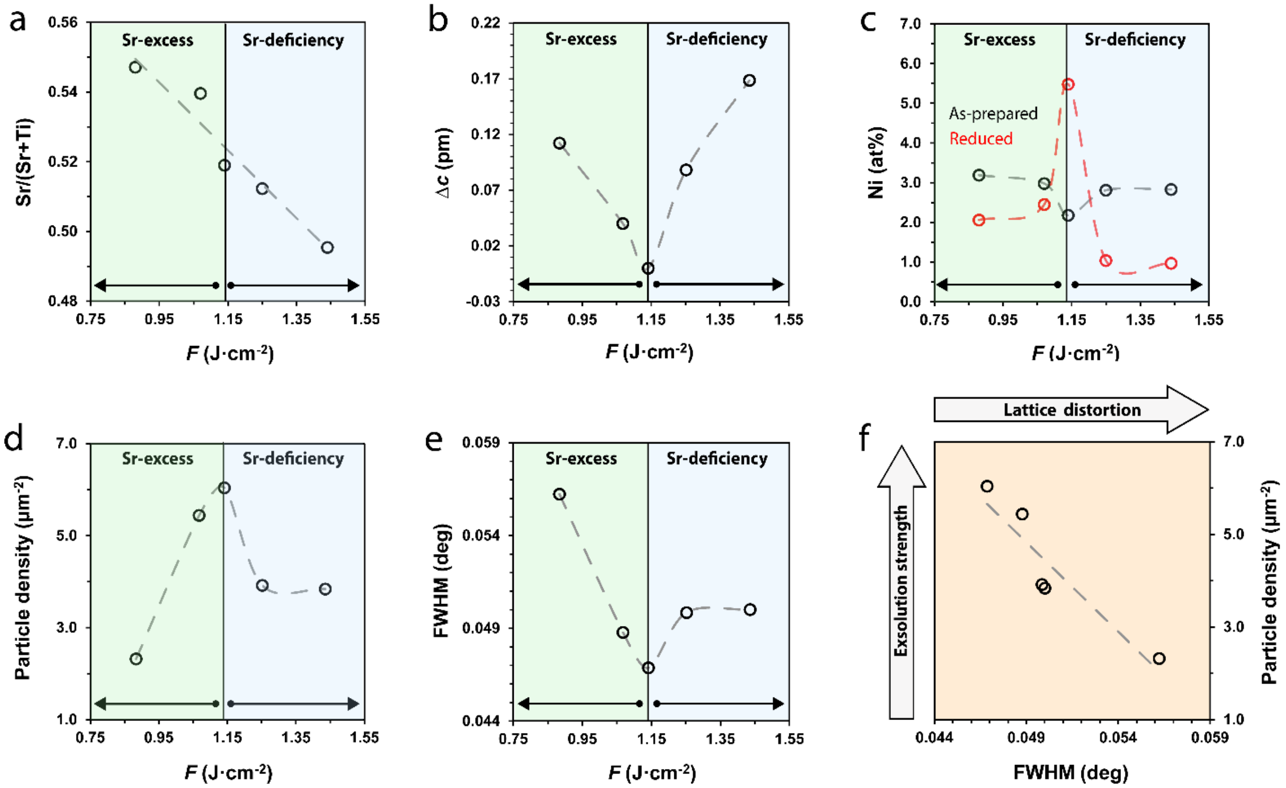

Figure 5. Evaluation of the exsolution behavior of Ni from epitaxial STNNi thin film model systems (annealing conditions: 15h / Ar/4% H_2 / 800°C). (a) Stoichiometry of the host lattice *i.e.* Sr/(Sr+Ti) ratio depending on the applied laser fluence. (b) Defect incorporation results in the expansion in the oxide *c*-lattice parameter relative to STNNi deposited at the stoichiometric point as determined by 2θ-ω scans around the (002) reflection. (c) Atomic concentration of Ni determined by XPS analysis relative to Sr, Ti and Nb in the as-prepared state (black symbols) and the reduced state of the samples (red symbols). A significant increase of the relative Nickel content in the near-surface region is observed for the stoichiometric sample after reducing treatment. (d) Particle density determined as additional indicator for exsolution strength as a function of laser fluence used to tune the Sr/(Sr+Ti) ratio, indicating strong exsolution for stoichiometric STNNi, while non-stoichiometry results in weak metal exsolution. (e) FWHM value as a function of laser fluence indicates the lowest degree of lattice distortion for stoichiometric STNNi, while non-stoichiometry results in accumulation of lattice imperfections. (f) Correlation between the average particle density at the crystal surface and the FWHM value determined by XRD rocking curve analysis serving as indicator for the distortion of the perovskite lattice. Low degree of lattice distortion results in strong metal exsolution while a high degree of lattice distortion hampers exsolution to the thin film surface, resulting in a lower particle density. A solid black line denotes the stoichiometric point; dashed lines serve as guide for the eye.

As can be seen from Fig. 5c off-stoichiometric thin film growth only has a minor effect on the Ni content for thin films deposited with varying laser fluence and hence small variations in Ni concentration can be neglected for the further discussion (black circular symbols). After reducing treatment, a significant increase in the relative Ni signal can be observed in the surface region of the thin films deposited at the stoichiometric point, while off-stoichiometric STNNi thin films exhibit a relative decrease of nickel in the surface region (red circular symbols).

Due to the inherent limitations of surface-sensitive XPS measurements for the quantification of inhomogeneous material systems such as lateral distributed nanoparticles (as discussed above)[52,53], particle density is determined as an additional indicator of exsolution strength for the evaluation and comparison of the exsolution behavior for STNNi thin films of different defect structure. For this purpose, a lower threshold of 10 nm was used to avoid overestimation in particle number due to surface decorations, which are likely to occur especially at surfaces of highly non-stoichiometric thin films. As shown in Fig. 5d, the highest particle densities are observed for STNNi thin films deposited close to the stoichiometric point, which is in good agreement with the results derived from XPS analysis. Consistent with literature, increasing Sr-excess results in suppressed metal exsolution[19], as reflected by the decrease in particle density. However, also Sr-deficiency results in a decreased number of nanoparticles appearing at the surface upon reduction.

Turning now to the structural analysis of the thin films, the influence of defect structures on the exsolution process is further highlighted. While the *c*-lattice expansion is a sensitive parameter for the extent of defect incorporation, the FWHM of rocking curve profiles is indicative for the lattice distortion of crystallographic planes[54–56] and hence, the relative degree of lattice distortion can be evaluated by XRD rocking curve analysis (cf. Fig. S9). Increasing distortion of the perovskite lattice results in a broadening of the rocking curves and respectively causes an increase in the FWHM value, which therefore may serve as a parameter to compare relative differences in atomic disorder. As evident from Fig. 5e, stoichiometric thin films exhibit the lowest degree of lattice distortion, while non-stoichiometry gives rise to lattice imperfections reflected by increased FWHM values, which is consistent with the accumulation of defects within the perovskite lattice compensating for non-stoichiometry. By plotting particle density against FWHM values the correlation between lattice distortion and particle density becomes more apparent (Fig. 5f). Evidently, Ni exsolution towards the thin film surface in epitaxial STNNi is strongly hampered by the distortion of crystallographic planes, which is directly related to the non-stoichiometry of the perovskite host lattice. Notably, a significant increase in lattice distortion is observed for the majority of thin films after the reducing treatment most likely connected to the formation of secondary phases within the thin film bulk (cf. Fig. S9).

Exsolution of embedded nanostructures.

Identifying ceramic STNNi as exsolution-active material, we followed a thin film approach to study the atomistic processes, which tailor the exsolution behavior of nickel nanoparticles in the material. Comprehensive characterization of epitaxial growth as well as surface and bulk properties allows for the synthesis of STNNi thin film models with considerably reduced complexity compared to their ceramic counterparts. Despite no secondary phases were detected by various characterization techniques, microscopic investigations revealed the presence of nanoscale features identified as Ni-rich structures embedded at designated regions of the as-synthesized perovskite host lattice. Similar (self-assembled) vertically aligned phases were reported to form during deposition of (composite) material systems fabricated by sequential ablation from different target materials.[43,57] In the case of STNNi, doping concentrations close to the solubility limit of Ni in STO[58,59] may favour partial phase separation from the strontium titanate host lattice and the spontaneous formation of Ni-rich secondary species. Although, no formation of secondary phases were observed for a series of sintered STNNi ceramics with substituted Ni concentrations below 10 % by XRD analysis. Nb-co-doping was chosen to provide sufficient electronic conductivity of the oxide matrix, which is required for catalytic activity. Note that throughout our experiments no hints on Nb-segregation or exsolution was found.

The observed nanostructures were identified to be most likely NiO_x phases, which reside in domain matching relationship within the perovskite host lattice based on the formation of a semicoherent interface. The reorganization of the crystal phase forming capsule-shaped Ni nanoclusters by undergoing a phase transition to the metallic state in the bulk of the film is evident after annealing at a temperature of $T = 800°C$, where cation diffusion should be in principle limited. Thus, a high mobility of the embedded nickel phase within the well-ordered strontium titanate host lattice is implied. Note, that temperatures of 800°C (and above) are commonly used for thin film annealing of (undoped) $SrTiO_3$ thin films[48,60,61] and in the typical temperature range of exsolution studies.[13-14,19,79] Since the size and shape of such embedded phases can be highly diverse and depend on the respective material system and synthesis conditions[43,62–65], their detection may require careful analysis on the nanoscale. Please note that the remaining Ni-doping level of the strontium titanate thin film is unclear, since considerable amounts of dopants are accumulated within the observed nanostructures.

Overall, these findings have two important implications (as summarized in Fig. 6): Firstly, exsolution-active materials may be not necessarily single-phase perovskites, but rather accommodate exsolving elements by local stoichiometry variations in the perovskite lattice on the nanometer scale before exsolution. The exsolution of such pre-formed nanoclusters is hence in contrast with the idealized concept of nanoparticle formation from a solid solution and furthermore must be considered as alternative pathway of mass transport during metal exsolution. This is of particular importance since cation segregation accompanied by the formation of dopant-rich secondary phases is commonly observed for a variety of mixed ionic and electronic conductors (MIEC) highly relevant for the application as exsolution-active materials.[66–73] Thus, a clear differentiation of potentially coexisting exsolution routes *i.e.* clustering of ions on the nanoscale previous to the transition to the metallic phase *versus* (thermally activated) clustering after reduction might prove difficult. Secondly, the synthesis of such composite materials allows to widely decouple nanoparticle nucleation (clustering of single atoms) from nanoparticle transport processes and hence enables the investigation of nanoparticle transport as (mostly) isolated event.

This approach was adopted to evaluate the influence of non-stoichiometry and respective defect structures on the mass transport during reducing treatment, revealing a clear correlation between lattice distortions of the host lattice due to the incorporation of defect structures and the efficient transport of nickel nanoparticles towards the surface. Here, the increased transport dynamics for stoichiometric thin films are reflected by an enhanced enrichment of the near-surface region with Ni as well as an increased particle density at the perovskite surface. Considering the well-known effect of A-site deficiency promoting metal exsolution the apparent detrimental effect of Sr-deficiency on Ni exsolution to the surface of epitaxial STNNi is surprising at first. However, it is likely to be connected to the pre-formed character of the nanoparticles and may help to further unravel the origin of stoichiometry effects on metal exsolution.

As depicted by Ref. [19], exsolution of B-site cations from an A-site deficient host perovskite is accompanied by the recovery of a stoichiometric host lattice, which is considered to serve as driving force for the spontaneous B-site exsolution and phase separation resulting in the nucleation of a B-site rich phase. The strategy behind the introduction of A-site deficiency to the perovskite host hence targets the destabilization of the perovskite structure on the unit cell level to increase the affinity towards spontaneous B-site exsolution. Starting with a material system of pre-formed nuclei, the pronounced transport of nickel to the oxide surface observed for the present material system at the stoichiometric point therefore is in good accordance with literature. Most importantly however, we find a detrimental effect of non-stoichiometry on the dynamics of metal exsolution reflected by a decreased particle density and decreased Ni enrichment in the near-surface region.

As discussed above this result is not in contrast to previous findings on the stoichiometry-effect on exsolution processes, but adds further insights on the effect of crystal defects on the dynamics of metal exsolution. Here, the driving force for exsolution of embedded nanostructures and from solid solution precursors is likely to be similar but the kinetics of nanoparticle nucleation and transport are fundamentally different. Therefore, the observed detrimental influence of A-site deficiency is most likely - however not exclusively - expected for the exsolution of pre-formed nuclei. The exact outcome of the introduction of A-site deficiency on the exsolution behavior is presumably determined by the interplay of the advantageous effect of A-site deficiency to promote nanoparticle nucleation and the disadvantageous effect of non-stoichiometry of the host lattice on the nanoparticle transport. Thus, a negative effect of non-stoichiometry may also come into play in the case of solid solution precursors depending on the extend of metal exsolution. Therefore, a well-balanced calibration of the amount of A-site vacancies *versus* the doping level may help to increase nanoparticle yield.

In summary two major findings, namely the observation of phase separation of dopant-rich nanosturctures serving as centers for the formation of metallic nanoparticles and the exsolution route-specific dopant transport dynamics have emerged from our analysis. For future work, it will be required to link these two aspects more closely, in order to understand how phase separation affects accompanying defect formation and *vice versa*. Please note, however, that the formation of self-assembled Ni-rich nanostructures was observed independent from thin film stoichiometry.

Our findings hence show that non-stoichiometry influences metal exsolution on the level of the particle transport. For metal exsolution starting from a solid solution of stoichiometric perovskite oxides, the resulting non-stoichiometry after B-site exsolution thus can be expected to hamper the transport of nanoparticles from the oxide bulk to the surface, commonly observed in form of decreased particle density. Nanoparticles formed in the oxide bulk may be trapped or slowed by designated defect structures limiting exsolution of nanoparticles to the oxide surface. Consistently, exsolved Ni nanoparticles were previously reported to be preferentially located in the vicinity of defect structures such as stacking faults in ceramic materials.[22]

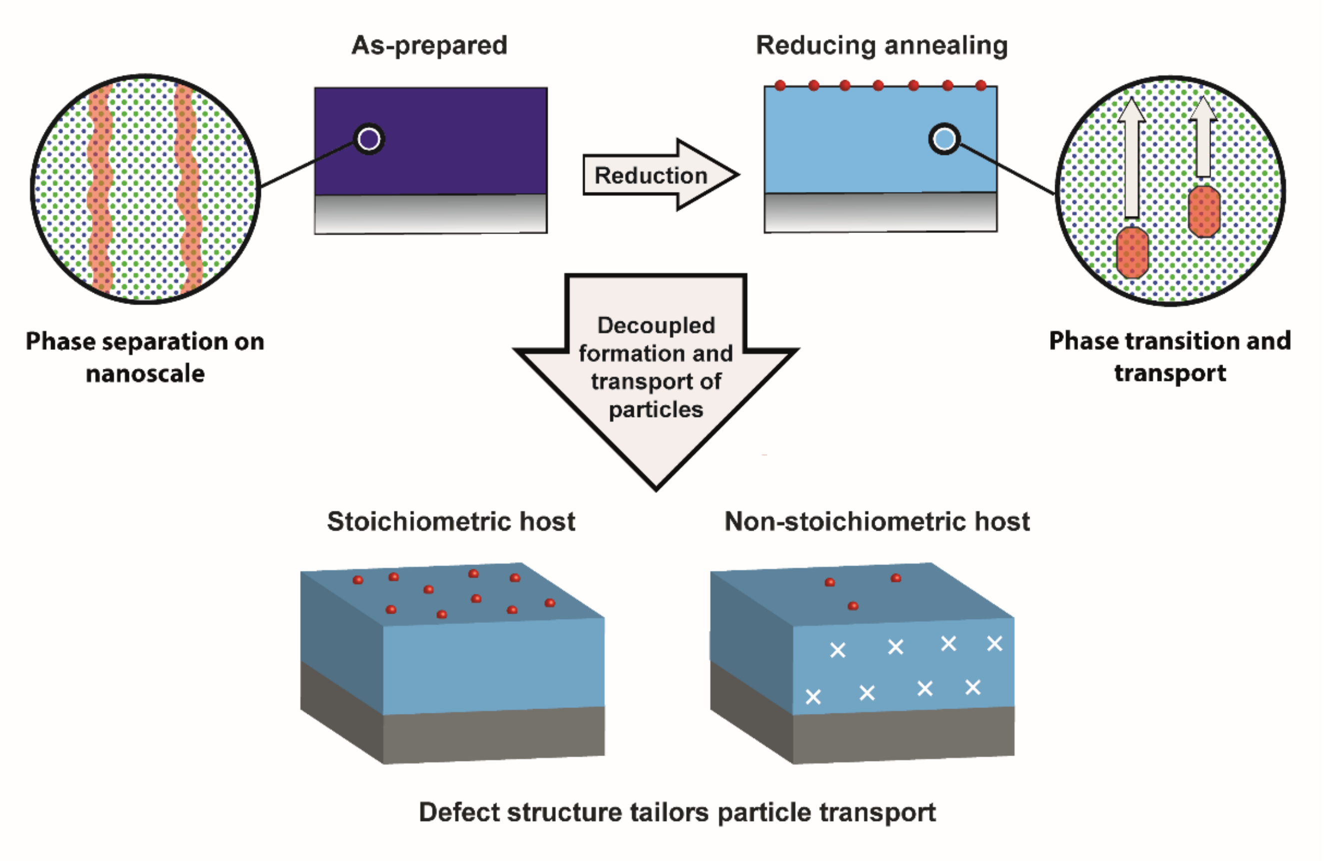

Figure 6. Schematic illustration of the exsolution process in STNNi model systems depending of thin film stoichiometry. Nickel-dopants tend to form nanostructures, embedded in the as-prepared perovskite host lattice and undergo a phase transition to the metallic state during reducing annealing which are transported to the thin film surface. Based on this concept, nanoparticle nucleation processes can be decoupled from particle transport. The highest particle density can be observed for stoichiometric thin films while the presence of defect structures hampers the transport Ni towards the surface and the formation of nickel nanoparticles. Ni-rich phases are denoted in in red; defect structures are illustrated by white crosses.

The successive incorporation of defects for non-stoichiometric STNNi in form of point defects and possibly large-volume defects such as point defect clusters, Ruddlesden-Popper-faults, TiO_x precipitates *etc.* causes severe distortions of the perovskite lattice with influence on various properties of the host lattice with potential impact on the nanoparticle-host interaction. For instance, Coulomb interactions of charged defects with (potentially charged) exsolving species or local strain fields induced by defect structures by displacing the atomic order may contribute to the trapping effect. Although the nature of the incorporated defects is expected to be different for Sr-rich and Sr-deficient crystal growth, the exsolution behavior is affected in a similar manner. This observation highlights that it may be not rational to expect one specific type of defect to tailor the overall behavior but that the degree of lattice distortion as a general parameter is more appropriate to describe the apparent relationship. The origin for the observed trapping effect on the scale of single defects however remains to be elucidated by further studies.

Lattice strain was not only shown to be one major driving force for cation segregation[53], but also found to play an essential role for mass transport of nanoparticles within the oxide host lattice during metal exsolution.[24,25] Here, transport of nanoparticles to the perovskite surface was reported to be based on the minimization of the elastic strain energy between the metallic phase and the surrounding oxide lattice as well as minimization of the surface free energy.[24,25] Major distortions of the perovskite host lattice might affect the exsolution process due to (local) deviations in lattice spacing and displacements of the atomic order. This may cause unfavourable strain interaction potentially affecting the directed transport of nanoparticles to the surface. The role of lattice strain however, remains unclear for the present material system since the respective crystallographic phases exhibit domain matching relationship and therefore only minor strain energies resulting from the residual misfit F_{CSL} are expected. Nevertheless, considerable deviations from the bulk lattice values of NiO and Ni were determined as depicted in Table S1. These may originate from the highly defective / distorted structure of the embedded phases (as-prepared state) or significant stresses resulting from the difference in elastic properties of the composite system.

The significance of the imperfection *i.e.* distortion of the host lattice is furthermore highlighted by the fact that a clear increase in the crystallinity of the embedded nanoclusters as well as an improved orientation relationship of the host lattice with the exsolving particles is visible after reducing annealing, which may be of high importance for the effective nanoparticle-host interaction during exsolution. The formation of precipitates in a defined lattice orientation relationship between nuclei and host lattice was reported to reduce the free energy of activation for the formation of nuclei in solids and hence may facilitate the accommodation of metallic Ni nanoclusters within the perovskite host matrix.[74] This observation is consistent with *in-Situ* studies of nanoparticle exsolution at surfaces of ceramic oxides which revealed an epitaxial relationship - and hence a defined orientation relationship - between the exsolved nanoparticles and the oxide host.[75] Here, defect structures displacing the atomic order are likely to restrict the structural relationship between the oxide host with the nanoparticles what might have significant influence on exsolution dynamics.

The high significance of the nanoparticle-host interface is also highlighted by ref.[76], discussing the migration mechanism of inclusions in solids. Here, migration of inclusions is explained by a diffusive flux of host cations along the inclusion-host interface (in the presence of an external gradient) allowing for the movement of the inclusion relative to the lattice of the host crystal within the respective cavity. This mechanism may be transferable to nanoparticle transport during metal exsolution. Consequently, the high mobility of exsolution nanoparticles might be determined by the mobility of cations of the host lattice (Sr, Ti, Nb), which may be significantly increased at the semi-coherent interface between oxide host and metallic nanoparticles and therefore enable nanoparticle transport at relatively low temperatures. The role of (semi-coherent) interfaces for the mobility of carriers however is controversially debated.[77]

Overall, the influence of the defect structure on the host-nanoparticle interaction is a highly complex issue. While various driving forces and parameters with influence on metal exsolution are known (as lately reviewed[78]), a universal driving force for the directed transport of nanoparticles towards the oxide surface and thus a conclusive mechanism of nanoparticle transport is still lacking. Therefore, extensive investigations will be necessary to gain a full picture of exsolution phenomena.

Our findings have important implications for the development of efficient exsolution materials since strategies for the control of nanoparticle properties may be - depending on exsolution route - essentially diverging. This might be of particular importance for highly A-site deficient perovskites, where B-site cations need to be stabilized at thermodynamically unfavourable crystallographic sites. For instance, limited effects of A-site deficiency[23] on the exsolution processes or non-reversibility of the process[79] reported in literature might be related to similar phenomena as described in the present study. For the synthesis of supported electrocatalysts *via* metal exsolution, control of the location of nanoparticle formation (bulk *vs.* surface) is of high interest since it determines accessibility of catalytically active nanoparticles and thus overall functionality and efficiency of the catalyst since nanoparticles which remain buried in the oxide bulk do not contribute in catalyzing electrochemical conversion reactions.[19,22,66,80]

Note that the observed phase separation may be seen as a feature of PLD-growth which corresponds to a non-equilibrium process. Typically, however, growth kinetics during epitaxy do not favor phase separation. In this case, a doping level close to the solubility level may furthermore contribute to favor phase separation during growth. Due to the inherent differences between bulk and thin film synthesis, a comparison should be made with great care.

CONCLUSION

We studied the redox exsolution behavior of Ni in STNNi based on dense epitaxial thin film model systems. A strong response to reducing thermal treatment resulting in the formation of homogeneously dispersed nanoparticles at the close-to atomically smooth (001) crystal face can be observed. Here, nanoparticle formation is accompanied by an enrichment of the thin film surface with nickel as well as a magnetic transition towards the ferromagnetic state and a relaxation of the crystal lattice collectively indicative for the phase transition and release of Ni-dopants to the perovskite surface in the form of metallic nanoparticles.

In conclusion, our results show that spontaneous phase separation on the nano-scale can result in the formation of Ni-rich nanostructures accommodated as secondary species within the as-synthesized perovskite lattice. Residing in domain matching relationship, these dopant-rich nanostructures serve as pre-formed nuclei for the subsurface formation of metallic nanoparticles and subsequent exsolution. Our findings hence demonstrate that different and possibly intermixed pathways of mass transport need to be considered to gain full understanding of the atomistic processes during nanoparticle formation at perovskite surfaces.

Based on this composite material system, the nanoparticle transport towards the perovskite surface may be decoupled from (diffusive) subsurface particle nucleation and particle growth processes and thus allows for the study of nanoparticle transport as mostly isolated process. The investigation of this unconventional exsolution route reveals a significant impact of non-stoichiometry on the exsolution efficiency, which is not based on the (well-known) influence on spontaneous phase separation, but affects nanoparticle transport dynamics. While stoichiometric thin films exhibit a low degree of lattice imperfections and a strong exsolution response, non-stoichiometry results in a considerable decrease of the particle density, which – as we show - is correlated to local distortions of the perovskite lattice. Our results may have major significance for the application of well-known and widely used concepts to control exsolution processes such as the synthesis of perovskite materials with high A site deficiency as precursors for nanostructured electrode materials *via* metal exsolution.

EXPERIMENTAL SECTION

Synthesis of powders and ceramics.

The $SrTi_{0.9}Nb_{0.05}Ni_{0.05}O_3$ (STNNi) oxide powders were prepared by the Pechini method. After dissolution of stoichiometric amounts of the educts (titanium(IV) isopropoxide (97 %) preprocessed as described by Ref. ([81]), strontium nitrate (99 %), ammonium niobate(V) oxalate hydrate (99.99 %) and nickel(II) nitrate hexahydrate (99.99 %)), metal ions were stabilized by complexation with citric acid and ethylene glycol was added. The solution was stirred for 24 h and at $T = 50°C$ and polymerization was induced by successive increase of temperature to $T = 350°C$. The product was calcined at $T = 700°C$ and $T = 900°C$ for 3 h respectively. A slurry of the powder (in isopropanol) was ball milled for 24 h and dried using a rotary evaporator. Ceramic pellets were uniaxially and cold-isostatically pressed using an organic binder (3.5 wt%) and sintered at $T = 1100°C$ for 6 h in air after debinding at $T = 600°C$ for 12 h. To determine cation stoichiometry of the PLD target a piece of the ceramic pellet was cut with a diamond wire saw and analyzed after fusion of the sample material with lithium borate in a Pt/Au crucible for 30 min at $T = 1000$ °C and subsequent dissolution of the mixture using HCl/H_2O_2 by inductively-coupled-plasma optical emission spectroscopy (ICP-OES, iCAP7600, Thermo Scientific, Massachusetts, USA). Ceramic $SrTi_{0.95-x}Nb_{0.05}Ni_xO_{3-\delta}$ pellets with varying nickel content of x = 0, 0.005, 0.01, 0.03, 0.05, 0.1 were prepared by the mixed-oxide route. Stoichiometric amounts of the educts (titanium(IV) oxide nanopowder (99.7 %), strontium carbonate (≥ 98 %), niobium(V) oxide (99.99 %) and nickel(II) oxide nanopowder (99.99 %)) were mixed and a slurry of the mixture (in isopropanol) was ball milled for 24 h to ensure homogeneous distribution of the compounds. After calcination at 1100°C for 8 h the powder was grinded by mortar and pestle and a slurry (in isopropanol) was ball milled for 24 h. The product was dried using a rotary evaporator and ceramic pellets were uniaxially and cold-isostatically pressed using an organic binder (3.5 wt%). After debinding at $T = 600°C$ for 12 h the pellets were sintered for 12 h at 1200°C. Crystal structure was investigated by X-ray diffraction (XRD, D4 Endeavor, Bruker, Massachusetts, USA). A slight signature of a NiO secondary phase associated with the Pechini fabrication route was detected for the ceramic PLD target, however it is not expected to influence thin film growth due to the atomization of involved species during target ablation. Microscopic analysis was performed after reducing annealing under constant gas flow (Ar / 4% H_2) for 5 h at $T = 800$ °C. The ceramic sample was investigated by secondary electron microscopy (SEM, SU 800, Hitachi High-Technologies Corporation, Japan) and by transmission electron microscopy (TEM, FEI Titan Tecnai G2 F20 S-Twin, Thermo Fisher Scientific, Hillsboro, USA) using an acccel-eration voltage of 200 kV) as well as energy dispersive X-ray spectroscopy (EDXS).

Epitaxy.

Epitaxial STNNi thin films with thicknesses of $t = 50$ nm were deposited by reflection high-energy electron diffraction (RHEED)-controlled pulsed laser deposition on one-side polished $SrTiO_3$ (STO) substrates (Shinkosha Co. Ltd., Yokohama, Japan) in [001] orientation. For this purpose, substrates were glued on *Omicron* holders using Ag-paste and kept at constant backside-temperature of $T = 730°C$ by an IR-diode laser with a wavelength of $\lambda = 925$ nm. The target material was ablated using a KrF excimer laser (Compex 205F, Coherent, Santa Clara, USA) with a wavelength of $\lambda = 248$ nm operated with a repetition rate of $f = 5$ Hz. The target-to-substrate distance was $d = 57$ mm. Epitaxial growth of thin films was performed at oxygen pressures of $p(O_2) = 0.110$ mbar. For the deposition of stoichiometric thin films a laser fluence of $F = 1.14\ J\cdot cm^{-2}$ was applied, while non-stoichiometric growth was induced by tuning the laser fluence between $F = 0.88 – 1.44\ J\cdot cm^{-2}$. After thin film growth, samples were annealed for ten minutes under deposition conditions and afterwards quenched down to room temperature. For exsolution studies, samples were annealed under constant gas flow (Ar / 4% H_2) for 15 h at $T = 800$ °C and quenched down to room temperature.

Thin film characterization.

Surface morphology was characterized by atomic force microscopy (AFM, Cypher, Oxford Instruments Asylum Research Inc., Santa Barbara, USA). Crystallographic properties were investigated by X-ray diffraction (XRD) analysis performing rocking curve analysis, standard XRD in Bragg-Brentano geometry as well as reciprocal space mapping (RSM) using an asymmetric scan geometry (D8 Discover, Bruker AXS GmbH, Karlsruhe, Germany). Cation distribution was investigated by depth profiling using time-of-flight secondary ion mass spectrometry (ToF-SIMS 5.NCS, IONTOF GmbH, Münster, Germany) in negative polarity mode. Relative surface stoichiometry was analyzed by X-ray photoelectron spectroscopy (XPS) recording the Sr3d-, Ti2p-, Nb3d-, and Ni2p- core-level spectra. XPS measurements were performed using Al $K_{\alpha1}$ line ($E_\lambda = 1486.6$ eV, FWHM = 0.26 eV) of a monochromized X-ray source and at a photoemission angle of $\Theta = 15°$ as well as constant pass energy ($E_0 = 29.35$ eV) in the fixed analyzer transmission mode (Phi 5000 VersaProbe, ULVAC Phi, Physical Electronics Inc.). For quantification, relative sensitivity factors (RSF) were referenced to the ceramic target material. For the analysis of the Sr/(Sr+Ti) ratio, quantification was performed in reference to a STO single-crystal. Binding energies of all spectra were aligned to the C 1s signal. For the analysis of bulk stoichiometry, [001]-oriented STNNi thin films were deposited on one-side polished $NdGaO_3$ substrates (CrysTec GmbH, Berlin, Germany) in orthorhombic (110) surface orientation. After dissolution in a mixture of HCl/H_2O_2 (volume ratio 3:1) for two hours at a temperature of $T = 50°C$, three aliquots of the solution were analyzed for each sample by inductively coupled plasma mass spectrometry (ICP-MS) (Agilent 7500ce). Magnetic measurements were performed using a vibrating sample magnetometer

(VSM) (Dynacool Physical Property Measurement System (PPMS) of Quantum Design). Full hysteresis loops between +/- 10 kOe were measured and a linear background was subtracted to correct for the diamagnetic contribution of the STO substrate.

High-angle annular dark-field imaging and corresponding energy dispersive X-ray spectroscopy were carried out in an FEI Titan G2 80-200 ChemiSTEM microscope equipped with a high-brightness field emission gun, a spherical aberration corrector for the probe forming lens and a super-X EDS system. The convergence semi-angle for HAADF imaging was about 25 mrad, while the collection semi-angle was 70-200 mrad. The TEM dark-field images and selected area electron diffraction patterns were recorded in an FEI Tecnai F20 microscope. Both microscopes were operated at 200 kV.

ASSOCIATED CONTENT

Supporting Information.
Figure S1, X-ray diffraction analysis of sintered $SrTi_{0.95-x}Nb_{0.05}Ni_xO_{3-\delta}$ ceramics with different level of Ni-substitution; Figure S2, TEM/EDXS analysis of a sintered ceramic STNNi pellet in the as-prepared state; Figure S3, wide-angle X-ray diffraction analysis of an epitaxial STNNi thin film in 2θ-ω geometry and comparison of reciprocal space maps (RSM) obtained from thin films in the as-prepared and the reduced state; Figure S4, representative XPS Sr3d-, Ti2p-, Ni2p- and Nb3d- core-level spectra obtained from STNNi thin films in the as-prepared state as well as Sr/(Sr+Ti) ratio for STNNi thin films deposited with different laser fluence determined by XPS and ICP-MS analysis; Figure S5, TEM/EDXS analysis of a representative stoichiometric STNNi thin film in the reduced state; Figure S6, fast-Fourier transforms of STEM Z-contrast images of STNNi thin films in the as-prepared and reduced state; Figure S7, simulated MOIRÉ patterns for superimposed crystal phases of bulk $SrTiO_3$ and NiO as well as $SrTiO_3$ and Ni; Figure S8 X-ray diffraction analysis of STNNi thin films in the (002) STNNi/STO region deposited with different laser fluence; Figure S9, XRD rocking curve analysis of STNNi thin films deposited with different laser fluence comparing the as-prepared and reduced state; Table S1, diffraction vectors *g* and lattice parameters *d* of the embedded phase (nanostructure) in the as-prepared and reduced state of the STNNi thin film obtained by SAED analysis. This material is available free of charge *via* the Internet at http://pubs.acs.org.

AUTHOR INFORMATION

Corresponding Author

*Moritz L. Weber, Christian Lenser, Felix Gunkel

Author Contributions

M. L. W. performed the sample synthesis and experiments unless not further specified, formal analysis, validation and interpretation, writing of the original draft including graphic design. M. W. performed VSM analysis, validation and interpretation. L. J. performed HR-TEM / SAED analysis, validation and interpretation. U. B. conducted SIMS analysis and validation. R. D, R. W., O. G., C. L. and F. G. supervised the research. C. L. and F. G. were involved in the interpretation of the results and the conceptualization of the study. C. L. and F. G. contributed equally to this work. All authors discussed and evaluated the results.

Funding Sources

The authors acknowledge funding by the Helmholtz Association.

ACKNOWLEDGMENT

The authors sincerely thank René Borowski, Volker Nischwitz, Kevin Kistermann, Sebastian Zischke and Cleopatra Herwartz for their experimental support. M.L.W. would like to thank Prof. Dr. Norbert Menzler for his valuable advice during the development of this research work.

REFERENCES

(1) Wachsman, E. D.; Marlowe, C. A.; Lee, K. T. Role of Solid Oxide Fuel Cells in a Balanced Energy Strategy. *Energy Environ. Sci.* **2012**, *5*, 5498–5509.

(2) Boldrin, P.; Brandon, N. P. Progress and Outlook for Solid Oxide Fuel Cells for Transportation Applications. *Nat Catal* **2019**, *2*, 571–577.

(3) Gómez, S. Y.; Hotza, D. Current Developments in Reversible Solid Oxide Fuel Cells. *Renewable and Sustainable Energy Reviews* **2016**, *61*, 155–174.

(4) Laguna-Bercero, M. A. Recent Advances in High Temperature Electrolysis Using Solid Oxide Fuel Cells: A Review. *Journal of Power Sources* **2012**, *203*, 4–16.

(5) Song, C. Fuel Processing for Low-Temperature and High-Temperature Fuel Cells Challenges, and Opportunities for Sustainable Development in the 21st Century. *Catalysis Today* **2002**, *77*, 17–49.

(6) Aricò, A. S.; Bruce, P.; Scrosati, B.; Tarancon, J.-M.; Van Schalkwijk, W.; Nanostructured Naterials for Advanced Energy Conversion and Storage Devices. *Nature materials* **2005**, *4*, 366–377.

(7) Mistry, H.; Varela, A. S.; Kühl, S.; Strasser, P.; Cuenya, B. R. Nanostructured Electrocatalysts with Tunable Activity and Selectivity. *Nat Rev Mater* **2016**, *1*.

(8) Chang, L. Y.; Barnard, A. S.; Gontard, L. C.; Dunin-Borkowski, R. E. Resolving the Structure of Active Sites on Platinum Catalytic Nanoparticles. *Nano letters* **2010**, *10*, 3073–3076.

(9) Sholklapper, T. Z.; Kurokawa, H.; Jacobson, C. P.; Visco, S. J.; Jonghe, L. C. de. Nanostructured Solid Oxide Fuel Cell Electrodes. *Nano Lett.* **2007**, *7*, 2136–2141.

(10) Celikbilek, O.; Thieu, C.-A.; Agnese, F.; Calì, E.; Lenser, C.; Menzler, N. H.; Son, J.-W.; Skinner, S. J.; Djurado, E. Enhanced Catalytic Activity of Nanostructured, A-Site Deficient $(La_{0.7}Sr_{0.3})_{0.95}(Co_{0.2}Fe_{0.8})O_{3-\delta}$ for SOFC Cathodes. *J. Mater. Chem. A* **2019**, *7*, 25102–25111.

(11) Zhi, M.; Lee, S.; Miller, N.; Menzler, N. H.; Wu, N. An Intermediate-Temperature Solid Oxide Fuel Cell with Electrospun Nanofiber Cathode. *Energy Environ. Sci.* **2012**, *5*, 7066.

(12) Thommy, L.; Joubert, O.; Hamon, J.; Caldes, M.-T. Impregnation versus Exsolution: Using Metal Catalysts to Improve Electrocatalytic Properties of LSCM-Based Anodes Operating at 600 °C. *International Journal of Hydrogen Energy* **2016**, *41*, 14207–14216.

(13) Neagu, D.; Oh, T.-S.; Miller, D. N.; Ménard, H.; Bukhari, S. M.; Gamble, S. R.; Gorte, R. J.; Vohs, J. M.; Irvine, J. T. S. Nano-Socketed Nickel Particles with Enhanced Coking Resistance Grown *in Situ* by Redox Exsolution. *Nature communications* **2015**, *6*, 8120.

(14) Sun, Y.-F.; Zhang, Y.-Q.; Chen, J.; Li, J.-H.; Zhu, Y.-T.; Zeng, Y.-M.; Amirkhiz, B. S.; Li, J.; Hua, B.; Luo, J.-L. New Opportunity for *in Situ* Exsolution of Metallic Nanoparticles on Perovskite Parent. *Nano Lett.* **2016**, *16*, 5303–5309.

(15) Arrivé, C.; Delahaye, T.; Joubert, O.; Gauthier, G. Exsolution of Nickel Nanoparticles at the Surface of a Conducting Titanate as Potential Hydrogen Electrode Material for Solid Oxide Electrochemical Cells. *Journal of Power Sources* **2013**, *223*, 341–348.

(16) Weber, M. L.; Ma, Q.; Meuffels, P.; Hensling, F. V. E.; Lenser, C.; Gunkel, F.; Menzler, N. H.; Dittmann, R.; Waser, R.; Guillon, O.

Development of Epitaxial Thin Film Model Electrodes for the Systematic Investigation of Metal Exsolution from MIEC Perovskite Oxides. *ECS Trans.* **2019**, *91*, 1783–1789.

(17) Nenning, A.; Fleig, J. Electrochemical XPS Investigation of Metal Exsolution on SOFC Electrodes: Controlling the Electrode Oxygen Partial Pressure in Ultra-High-Vacuum. *Surface Science* **2019**, *680*, 43–51.

(18) Myung, J.-H.; Neagu, D.; Miller, D. N.; Irvine, J. T. S. Switching on Electrocatalytic Activity in Solid Oxide Cells. *Nature* **2016**, *537*, 528–531.

(19) Neagu, D.; Tsekouras, G.; Miller, D. N.; Ménard, H.; Irvine, J. T. S. *In Situ* Growth of Nanoparticles Through Control of Non-Stoichiometry. *Nature chemistry* **2013**, *5*, 916–923.

(20) Gao, Y.; Chen, D.; Saccoccio, M.; Lu, Z.; Ciucci, F. From Material Design to Mechanism Study: Nanoscale Ni Exsolution on a Highly Active A-Site Deficient Anode Material for Solid Oxide Fuel Cells. *Nano Energy* **2016**, *27*, 499–508.

(21) Sun, Y.; Li, J.; Zeng, Y.; Amirkhiz, B. S.; Wang, M.; Behnamian, Y.; Luo, J. A-Site Deficient Perovskite: the Parent for *in Situ* Exsolution of Highly Active, Regenerable Nano-Particles as SOFC Anodes. *J. Mater. Chem. A* **2015**, *3*, 11048–11056.

(22) Singh, S.; Prestat, E.; Huang, L.-F.; Rondinelli, J. M.; Haigh, S. J.; Rosen, B. A. Role of 2D and 3D Defects on the Reduction of LaNiO$_3$ Nanoparticles for Catalysis. *Scientific reports* **2017**, *7*, 10080.

(23) Zhu, T.; Troiani, H.; Mogni, L. V.; Santaya, M.; Han, M.; Barnett, S. A. Exsolution and Electrochemistry in Perovskite Solid Oxide Fuel Cell Anodes: Role of Stoichiometry in Sr(Ti,Fe,Ni)O$_3$. *Journal of Power Sources* **2019**, *439*, 227077.

(24) Han, H.; Park, J.; Nam, S. Y.; Kim, K. J.; Choi, G. M.; Parkin, S. S. P.; Jang, H. M.; Irvine, J. T. S. Lattice Strain-Enhanced Exsolution of Nanoparticles in Thin Films. *Nature communications* **2019**, *10*, 1471.

(25) Oh, T.-S.; Rahani, E. K.; Neagu, D.; Irvine, J. T. S.; Shenoy, V. B.; Gorte, R. J.; Vohs, J. M. Evidence and Model for Strain-Driven Release of Metal Nanocatalysts from Perovskites During Exsolution. *The journal of physical chemistry letters* **2015**, *6*, 5106–5110.

(26) Ma, Q.; Tietz, F.; Sebold, D.; Stöver, D. Y-Substituted SrTiO$_3$–YSZ Composites as Anode Materials for Solid Oxide Fuel Cells: Interaction Between SYT and YSZ. *Journal of Power Sources* **2010**, *195*, 1920–1925.

(27) Ma, Q.; Iwanschitz, B.; Dashjav, E.; Baumann, S.; Sebold, D.; Arul Raj, I.; Mai, A.; Tietz, F. Microstructural Variations and their Influence on the Performance of Solid Oxide Fuel Cells Based on Yttrium-Substituted Strontium Titanate Ceramic Anodes. *Journal of Power Sources* **2015**, *279*, 678–685.

(28) Holtappels, P.; Irvine, J. T. S.; Iwanschitz, B.; Kuhn, L. T.; Lu, L.; Ma, Q.; Malzbender, J.; Mai, A.; Ramos, T.; Rass-Hansen, J.; Sudireddy, B. R.; Tietz, F.; Vasechko, V.; Veltzé, S.; Verbraeken, M. Full Ceramic Fuel Cells Based on Strontium Titanate Anodes, an Approach Towards More Robust SOFCs. *ECS Trans.* **2013**, *57*, 1175–1184.

(29) Rodenbücher, C.; Luysberg, M.; Schwedt, A.; Havel, V.; Gunkel, F.; Mayer, J.; Waser, R. Homogeneity and Variation of Donor Doping in Verneuil-Grown SrTiO$_3$:Nb Single Crystals. *Scientific reports* **2016**, *6*, 32250.

(30) Brooks, C. M.; Kourkoutis, L. F.; Heeg, T.; Schubert, J.; Muller, D. A.; Schlom, D. G. Growth of Homoepitaxial SrTiO$_3$ Thin Films by Molecular-Beam Epitaxy. *Appl. Phys. Lett.* **2009**, *94*, 162905.

(31) Wiedigen, S.; Kramer, T.; Feuchter, M.; Knorr, I.; Nee, N.; Hoffmann, J.; Kamlah, M.; Volkert, C. A.; Jooss, C. Interplay of Point Defects, Biaxial Strain, and Thermal Conductivity in Homoepitaxial SrTiO$_3$ Thin Films. *Appl. Phys. Lett.* **2012**, *100*, 61904.

(32) Tokuda, Y.; Kobayashi, S.; Ohnishi, T.; Mizoguchi, T.; Shibata, N.; Ikuhara, Y.; Yamamoto, T. Growth of Ruddlesden-Popper Type Faults in Sr-Excess SrTiO $_3$ Homoepitaxial Thin Films by Pulsed Laser Deposition. *Appl. Phys. Lett.* **2011**, *99*, 173109.

(33) Suzuki, T.; Nishi, Y.; Fujimoto, M. Defect Structure in Homoepitaxial Non-Stoichiometric Strontium Titanate Thin Films. *Philosophical Magazine A* **2000**, *80*, 621–637.

(34) Swallow, J. G.; Woodford, W. H.; Chen, Y.; Lu, Q.; Kim, J. J.; Chen, D.; Chiang, Y.-M.; Carter, W. C.; Yildiz, B.; Tuller, H. L.; Van Vliet, K. J. Chemomechanics of Ionically Conductive Ceramics for Electrical Energy Conversion and Storage. *J Electroceram* **2014**, *32*, 3–27.

(35) Perry, N. H.; Kim, J. J.; Bishop, S. R.; Tuller, H. L. Strongly Coupled Thermal and Chemical Expansion in the Perovskite Oxide System Sr(Ti,Fe)O$_{3-\alpha}$. *J. Mater. Chem. A* **2015**, *3*, 3602–3611.

(36) Tinti, V. B.; Marani, D.; Ferlauto, A. S.; Fonseca, F. C.; Esposito, V.; Florio, D. Z. Exsolution of Nickel Nanoparticles from Mixed-Valence Metal Oxides: A Quantitative Evaluation by Magnetic Measurements. *Part. Part. Syst. Charact.* **2020**, *37*, 1900472.

(37) Roy, A.; Toro, J. A. de; Amaral, V. S.; Muniz, P.; Riveiro, J. M.; Ferreira, J. M. F. Exchange Bias Beyond the Superparamagnetic Blocking Temperature of the Antiferromagnet in a Ni-NiO Nanoparticulate System. *Journal of Applied Physics* **2014**, *115*, 73904.

(38) Makhlouf, S. A.; Parker, F. T.; Spada, F. E.; Berkowitz, A. E. Magnetic Anomalies in NiO Nanoparticles. *Journal of Applied Physics* **1997**, *81*, 5561–5563.

(39) Tadic, M.; Nikolic, D.; Panjan, M.; Blake, G. R. Magnetic Properties of NiO (Nickel Oxide) Nanoparticles: Blocking Temperature and Neel Temperature. *Journal of Alloys and Compounds* **2015**, *647*, 1061–1068.

(40) Kim, K. J.; Han, H.; Defferriere, T.; Yoon, D.; Na, S.; Kim, S. J.; Dayaghi, A. M.; Son, J.; Oh, T.-S.; Jang, H. M.; Choi G. M. Facet-Dependent *in Situ* Growth of Nanoparticles in Epitaxial Thin Films: The Role of Interfacial Energy. *Journal of the American Chemical Society* **2019**, *141*, 7509–7517.

(41) Jin, L.; Zapf, M.; Stübinger, M.; Kamp, M.; Sing, M.; Claessen, R.; Jia, C.-L. Atomic-Scale Interface Structure in Domain Matching Epitaxial BaBiO$_3$ Thin Films Grown on SrTiO$_3$ Substrates. *Phys. Status Solidi RRL* **2020**, *14*, 2000054.

(42) Trampert, A.; Ploog, K. H. Heteroepitaxy of Large-Misfit Systems: Role of Coincidence Lattice. *Cryst. Res. Technol.* **2000**, *35*, 793–806.

(43) Chen, A.; Hu, J.-M.; Lu, P.; Yang, T.; Zhang, W.; Li, L.; Ahmed, T.; Enriquez, E.; Weigand, M.; Su, Q.; Haiyan, W.; Zhu, J.-X.; MacManus-Driscoll, J. L.; Chen, L.-Q.; Yarotski, D.; Jia, Q. Role of Scaffold Network in Controlling Strain and Functionalities of Nanocomposite Films. *Science advances* **2016**, *2*, e1600245.

(44) Lu, L.; Wang, J.; Zheng, H.; Zhao, D.; Wang, R.; Gui, J. Spontaneous Formation of Filamentary Cd Whiskers and Degradation of CdMgYb Icosahedral Quasicrystal Under Ambient Conditions. *J. Mater. Res.* **2012**, *27*, 1895–1904.

(45) Dittmann, R. Stoichiometry in Epitaxial Oxide Thin Films. *Epitaxial Growth of Complex Metal Oxides*; Elsevier, 2015; pp 231–261.

(46) Wicklein, S.; Sambri, A.; Amoruso, S.; Wang, X.; Bruzzese, R.; Koehl, A.; Dittmann, R. Pulsed Laser Ablation of Complex Oxides: The Role of Congruent Ablation and Preferential Scattering for the Film Stoichiometry. *Appl. Phys. Lett.* **2012**, *101*, 131601.

(47) Keeble, D. J.; Wicklein, S.; Dittmann, R.; Ravelli, L.; Mackie, R. A.; Egger, W. Identification of A- and B-Site Cation Vacancy Defects in Perovskite Oxide Thin Films. *Physical review letters* **2010**, *105*, 226102.

(48) Gunkel, F.; Wicklein, S.; Hoffmann-Eifert, S.; Meuffels, P.; Brinks, P.; Huijben, M.; Rijnders, G.; Waser, R.; Dittmann, R. Transport Limits in Defect-Engineered LaAlO$_3$/SrTiO$_3$ Bilayers. *Nanoscale* **2015**, *7*, 1013–1022.

(49) Ohnishi, T.; Lippmaa, M.; Yamamoto, T.; Meguro, S.; Koinuma, H. Improved Stoichiometry and Misfit Control in Perovskite Thin Film Formation at a Critical Fluence by Pulsed Laser Deposition. *Appl. Phys. Lett.* **2005**, *87*, 241919.

(50) Breckenfeld, E.; Shah, A. B.; Martin, L. W. Strain Evolution in Non-Stoichiometric Heteroepitaxial Thin-Film Perovskites. *J. Mater. Chem. C* **2013**, *1*, 8052.

(51) Xu, C.; Du, H.; van der Torren, A. J. H.; Aarts, J.; Jia, C.-L.; Dittmann, R. Formation Mechanism of Ruddlesden-Popper-Type Antiphase Boundaries During the Kinetically Limited Growth of Sr Rich $SrTiO_3$ Thin Films. *Scientific reports* **2016**, *6*, 38296.

(52) Andrä, M.; Bluhm, H.; Dittmann, R.; Schneider, C. M.; Waser, R.; Mueller, D. N.; Gunkel, F. Chemical Control of the Electrical Surface Properties in Donor-Doped Transition Metal Oxides. *Phys. Rev. Materials* **2019**, *3*, 044604.

(53) Lee, W.; Han, J. W.; Chen, Y.; Cai, Z.; Yildiz, B. Cation Size Mismatch and Charge Interactions Drive Dopant Segregation at the Surfaces of Manganite Perovskites. *Journal of the American Chemical Society* **2013**, *135*, 7909–7925.

(54) Zhang-Yin, Z.; Xiao-Shan, W.; Quan-Jie, J. High resolution X-Ray Diffraction Investigation of Epitaxially Grown $SrTiO_3$ Thin Films by Laser-MBE. *Chinese Phys. C* **2009**, *33*, 949–953.

(55) Patterson, E. A.; Major, M.; Donner, W.; Durst, K.; Webber, K. G.; Rödel, J. Temperature-Dependent Deformation and Dislocation Density in $SrTiO_3$ (001) Single Crystals. *J American Ceramic Society* **2016**, *99*, 3411–3420.

(56) Zhai, Z. Y.; Wu, X. S.; Cai, H. L.; Lu, X. M.; Hao, J. H.; Gao, J.; Tan, W. S.; Jia, Q. J.; Wang, H. H.; Wang, Y. Z. Dislocation Density and Strain Distribution in $SrTiO_3$ Film Grown on (1 1 0) $DyScO_3$ Substrate. *J. Phys. D: Appl. Phys.* **2009**, *42*, 105307.

(57) MacManus-Driscoll, J. L.; Zerrer, P.; Wang, H.; Yang, H.; Yoon, J.; Fouchet, A.; Yu, R.; Blamire, M. G.; Jia, Q. Strain Control and Spontaneous Phase Ordering in Vertical Nanocomposite Heteroepitaxial Thin Films. *Nature materials* **2008**, *7*, 314–320.

(58) Beale, A. M.; Paul, M.; Sankar, G.; Oldman, R. J.; Catlow, C. R. A.; French, S.; Fowles, M. Combined Experimental and Computational Modelling Studies of the Solubility of Nickel in Strontium Titanate. *J. Mater. Chem.* **2009**, *19*, 4391.

(59) Sluchinskaya, I. A.; Lebedev, A. I.; Erko, A. Structural Position and Oxidation State of Nickel in $SrTiO_3$. *J. Adv. Dielect.* **2013**, *03*, 1350031.

(60) De Souza, R. A.; Gunkel, F.; Hoffmann-Eifert, S.; Dittmann, R. Finite-Size Versus Interface-Proximity Effects in Thin-Film Epitaxial $SrTiO_3$. *Phys. Rev. B* **2014**, *89*, 241401(R).

(61) Kozuka, Y.; Hikita, Y.; Bell, C.; Hwang, H. Y. Dramatic Mobility Enhancements in Doped $SrTiO_3$ Thin Films by Defect Management. *Appl. Phys. Lett.* **2010**, *97*, 12107.

(62) Zheng, H.; Wang, J.; Lofland, S. E.; Ma, Z.; Mohaddes-Ardabili, L.; Zhao, T.; Salamanca-Riba, L.; Shinde, S. R.; Ogale, S. B.; Bai, F.; Viehland, D.; Jia, Y.; Schlom, D. G.; Wuttig, M.; Roytburd, A.; Ramesh, R. Multiferroic $BaTiO_3$-$CoFe_2O_4$ Nanostructures. *Science (New York, N.Y.)* **2004**, *303*, 661–663.

(63) Zheng, H.; Zhan, Q.; Zavaliche, F.; Sherburne, M.; Straub, F.; Cruz, M. P.; Chen, L.-Q.; Dahmen, U.; Ramesh, R. Controlling Self-Assembled Perovskite-Spinel Nanostructures. *Nano Lett.* **2006**, *6*, 1401–1407.

(64) Moshnyaga, V.; Damaschke, B.; Shapoval, O.; Belenchuk, A.; Faupel, J.; Lebedev, O. I.; Verbeeck, J.; van Tendeloo, G.; Mücksch, M.; Tsurkan, V.; Tidecks, R.; Samwer, K. Structural Phase Transition at the Percolation Threshold in Epitaxial $(La_{0.7}Ca_{0.3}MnO_3)_{1-x}$:$(MgO)_x$ Nanocomposite Films. *Nature materials* **2003**, *2*, 247–252.

(65) Lee, S.; Zhang, W.; Khatkhatay, F.; Jia, Q.; Wang, H.; MacManus-Driscoll, J. L. Strain Tuning and Strong Enhancement of Ionic Conductivity in $SrZrO_3$-RE_2O_3 (RE = Sm, Eu, Gd, Dy, and Er) Nanocomposite Films. *Adv. Funct. Mater.* **2015**, *25*, 4328–4333.

(66) Lee, J. G.; Myung, J.-H.; Naden, A. B.; Jeon, O. S.; Shul, Y. G.; Irvine, J. T. S. Perovskites: Replacement of Ca by Ni in a Perovskite Titanate to Yield a Novel Perovskite Exsolution Architecture for Oxygen-Evolution Reactions (Adv. Energy Mater. 10/2020). *Adv. Energy Mater.* **2020**, *10*, 2070044.

(67) Desu, S. B.; Payne, D. A. Interfacial Segregation in Perovskites: II, Experimental Evidence. *J American Ceramic Society* **1990**, *73*, 3398–3406.

(68) Knauer, U. Distribution of the Iron Dopant in Barium Titanate Ceramic, Determined by the Scanning Transmission Electron Microscope. *Phys. Stat. Sol. (a)* **1979**, *53*, 207–210.

(69) Ernst, F.; Kienzle, O.; Rühle, M. Structure and Composition of Grain Boundaries in Ceramics. *Journal of the European Ceramic Society* **1999**, *19*, 665–673.

(70) Cai, Z.; Kubicek, M.; Fleig, J.; Yildiz, B. Chemical Heterogeneities on $La_{0.6}Sr_{0.4}CoO_{3-\delta}$ Thin Films—Correlations to Cathode Surface Activity and Stability. *Chem. Mater.* **2012**, *24*, 1116–1127.

(71) Konysheva, E. Y.; Xu, X.; Irvine, J. T. S. On the Existence of A-Site Deficiency in Perovskites and Its Relation to the Electrochemical Performance. *Advanced materials (Deerfield Beach, Fla.)* **2012**, *24*, 528–532.

(72) Horvath, G.; Gerblinger, J.; Meixner, H.; Giber, J. Segregation Driving Forces in Perovskite Titanates. *Sensors and Actuators B: Chemical* **1996**, *32*, 93–99.

(73) Zhao, Y. G.; Li, Y. H.; Ogale, S. B.; Rajeswari, M.; Smolyaninova, V.; Wu, T.; Biswas, A.; Salamanca-Riba, L.; Greene, R. L.; Ramesh, R.; Venkatesan, T.; Scott, J. H. Electrical Transport and Magnetic Properties of a Possible Electron-Doped Layered Manganese Oxide. *Phys. Rev. B* **2000**, *61*, 4141–4145.

(74) Johnson, W. C.; White, C. L.; Marth, P. E.; Ruf, P. K.; Tuominen, S. M.; Wade, K. D.; Russell, K. C.; Aaronson, H. I. Influence of Crystallography on Aspects of Solid-Solid Nucleation Theory. *Metallurgical Transactions A* **1975**, *6*, 911.

(75) Neagu, D.; Kyriakou, V.; Roiban, I.-L.; Aouine, M.; Tang, C.; Caravaca, A.; Kousi, K.; Schreur-Piet, I.; Metcalfe, I. S.; Vernoux, P.; an de Sanden, M. C. M.; Tsampas, M. N. *In Situ* Observation of Nanoparticle Exsolution from Perovskite Oxides: From Atomic Scale Mechanistic Insight to Nanostructure Tailoring. *ACS nano* **2019**, *13*, 12996–13005.

(76) Geguzin, J. E.; Krivoglaz, M. A. *Migration of Macroscopic Inclusions in Solids*; Studies in Soviet science; Consultants Bureau: New York, 1973.

(77) Uberuaga, B. P.; Dholabhai, P. P.; Pilania, G.; Chen, A. Semicoherent Oxide Heterointerfaces: Structure, Properties, and Implications. *APL Materials* **2019**, *7*, 100904.

(78) Kwon, O.; Joo, S.; Choi, S.; Sengodan, S.; Kim, G. Review on Exsolution and Its Driving Forces in Perovskites. *J. Phys. Energy* **2020**, *2*, 32001.

(79) Neagu, D.; Papaioannou, E. I.; Ramli, W. K. W.; Miller, D. N.; Murdoch, B. J.; Ménard, H.; Umar, A.; Barlow, A. J.; Cumpson, P. J.; Irvine, J. T. S.; Metcalfe, I. S. Demonstration of Chemistry at a Point Through Restructuring and Catalytic Activation at Anchored Nanoparticles. *Nature communications* **2017**, *8*, 1855.

(80) Katz, M. B.; Zhang, S.; Duan, Y.; Wang, H.; Fang, M.; Zhang, K.; Li, B.; Graham, G. W.; Pan, X. Reversible Precipitation/Dissolution of Precious-Metal Clusters in Perovskite-Based Catalyst Materials: Bulk Versus Surface Re-Dispersion. *Journal of Catalysis* **2012**, *293*, 145–148.

(81) Ma, Q.; Tietz, F.; Leonide, A.; Ivers-Tiffée, E. Electrochemical Performances of Solid Oxide Fuel Cells Based on Y-Substituted $SrTiO_3$ Ceramic Anode Materials. *Journal of Power Sources* **2011**, *196*, 7308–7312.

Insert Table of Contents artwork here